Quantitative Characterization of Sphere-Templated Porous Biomaterials

A. J. Marshall and B. D. Ratner
University of Washington Engineered Biomaterials, University of Washington, Seattle, WA 98195

DOI 10.1002/aic.10390
Published online March 3, 2005 in Wiley InterScience (www.interscience.wiley.com).

Three-dimensional (3-D) porous hydrogels were fabricated by polymerizing 2-hydroxyethyl methacrylate around templates of random close-packed poly(methyl methacrylate) microspheres with nominal diameter of 5 or 15 μm. The templates were leached out to create networks of interconnected spherical pores. Applications for sphere-templated porous biomaterials include scaffolds for tissue engineering and spatial control of wound healing. This study describes an approach to characterizing pore structure and predicting permeability of sphere-templated porous hydrogels. The materials were embedded in resin, and 1-μm-plane sections were digitally analyzed with fluorescence microscopy. The porosity and pore size distribution were determined from stereological interpretation, and we present novel techniques for obtaining the pore throat size distribution, the number of pore throats per pore, and the tortuosity. A simple apparatus is also introduced for measurement of the hydraulic permeability. Permeability predictions based on quantitative microscopy measurements and on stereology were found to agree closely with permeability measurements. The aptness of the Kozeny equation for spherically pored materials is also investigated. © 2005 American Institute of Chemical Engineers *AIChE J,* 51: 1221–1232, 2005

Keywords: quantitative microscopy, porous media, stereology, tortuosity, permeability

Introduction

Sphere-templating techniques permit the fabrication of porous materials with networks of interconnected spherical voids. The general method involves filling the interstitial space between packed spherical porogens with a fluid that is subsequently solidified into a skeleton. The porogens are then removed under conditions that leave the framework intact. Figure 1 shows scanning electron micrographs of sphere-templated porous hydrogel materials with pore structures constituting networks of interconnected spherical voids. Similar porous structures can be achieved with gas foaming (Harris et al., 1998) or phase separation (Hua et al., 2002) techniques. If solid spherical porogens are used, the size of the pore throats (that is, the windows that connect neighboring pores) can be tuned by sintering the spheres before addition of the skeleton precursor (Ma and Choi, 2001).

With well-defined pore geometry as well as controllable pore size, sphere-templated porous materials are attractive candidates for tissue engineering, where pore size must be carefully controlled. The importance of controlled implant pore size is demonstrated by experiments suggesting examples such as optimum pore size of 5 μm for neovascularization, 5–15 μm for fibroblast ingrowth, about 20 μm for hepatocyte ingrowth, and 20–125 μm for regeneration of adult mammalian skin (Yang et al., 2001). With a growing emphasis on pore size and other pore structural parameters, the need for accurate methods for quantitative characterization of porous materials has come to the forefront.

As Figure 1 suggests, scanning electron microscopy (SEM) is a valuable tool for viewing microscopic pore structures in three dimensions, but its use as a quantitative analysis tool is limited. For quantitative measurements of pore-structural parameters such as pore size distribution and pore throat size

Correspondence concerning this article should be addressed to B. D. Ratner at ratner@uweb.engr.washington.edu.

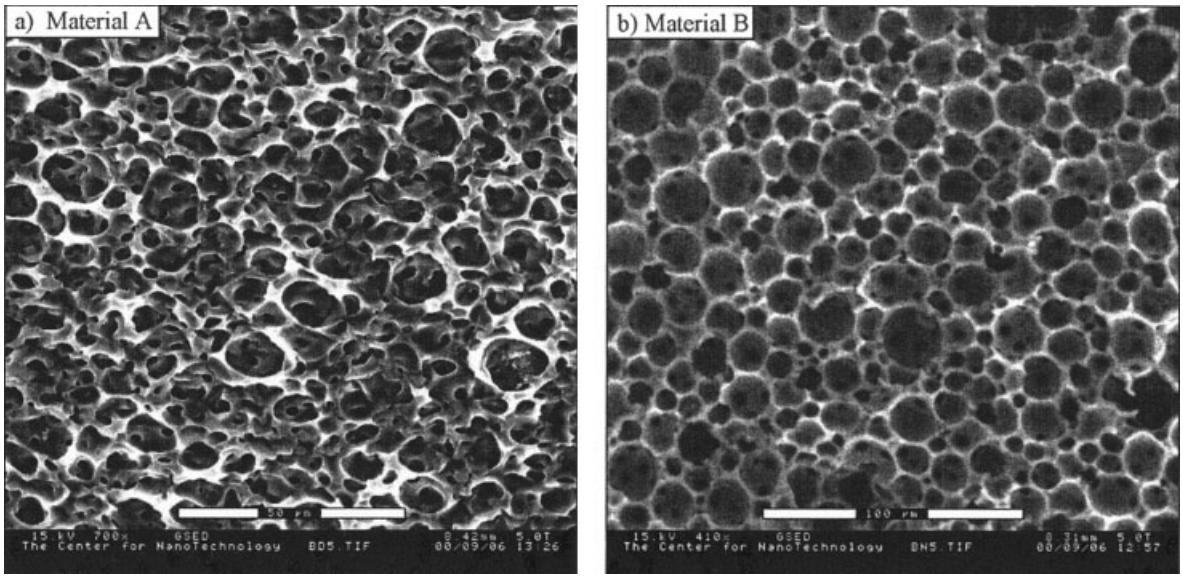

Figure 1. Scanning electron micrographs of sphere-templated porous poly(2-hydroxyethyl methacrylate) hydrogels (Marshall and Ratner, 2001).

Note that dehydrated pores are about 85% of hydrated size: (a) spherical porogens (~5 μm), cross section cut before porogens removed; (b) spherical porogens (~15 μm), cross section cut after porogens removed.

distribution, most researchers turn to mercury intrusion porosimetry, gas adsorption, or other pore-structural probing techniques. Although such techniques are useful for approximating some key pore properties, such as the pore-throat size distribution and the porosity, the exactness of the measurements obtained can be compromised by heavy reliance on various assumptions in the modeling (Yortsos, 1999).

One simple approach to pore structure characterization of sphere-templated materials involves measurement of the size distribution of the porogens. In some cases, the porogen size distribution can be used along with the mass density of the porogen particles to determine the porosity, pore size distribution, and number of pores per unit volume. However, this approach has limited utility if the material that constitutes the porogens absorbs an appreciable amount of the solvent used for the templated phase.

The symmetry and uniform pore geometry of sphere-templated porous materials suggest that the pore structures can be characterized with a higher degree of quantitative accuracy. In fact, this class of porous materials is especially well suited to analysis by quantitative microscopy. The geometric properties of the three-dimensional pore structures of these materials can be determined stereologically by analyzing two-dimensional sections. Figure 2 shows fluorescence micrographs of a thin section of each porous material presented in Figure 1, produced by flooding the pores with fluorescent dye, embedding in epoxy resin, and sectioning with a microtome.

The technique of sphere unfolding, in which the number and size distribution of spheres arranged randomly in three-dimensional space are statistically determined from analysis of a two-dimensional section, was developed nearly a century ago (Wicksell, 1925). This study takes the technique a step further; we demonstrate a method to determine pore throat size distributions in materials composed of interconnected spherical voids.

Tortuosity is an important transport property because its value must be known to quantitatively relate pore size to permeability. If we consider a slab of porous material with thickness L, we can define the tortuosity α by the following equation, where L_e is the relative average length of the flow path of a fluid particle from one side of the porous medium to the other (Wong, 1999),

$$\alpha = \left(\frac{L_e}{L}\right)^2 \tag{1}$$

The tortuous effective path length L_e always exceeds the straight-line path length L, so α is a dimensionless quantity with a value always >1. To avoid confusion when comparing tortuosity values for materials, it should be noted that this definition of tortuosity is not universal because some authors (for example, Collins, Scheidegger, and Bear) choose an alternative convention by instead defining the tortuosity as L_e/L.

Tortuosity is a difficult transport property to measure. It is possible to determine the tortuosity of a porous medium by saturating a sample with ionic solution, and then comparing the resistivity of the saturated sample to the bulk resistivity of the same ionic solution. However, the electrical conductivity of a sample is not necessarily equivalent to the hydraulic conductivity. Moreover, this type of electrical measurement is cumbersome to set up experimentally, with large and precise sample shapes required for accuracy (Collins, 1961). In this report, we present a method for determining the tortuosity from stereological interpretation of quantitative microscopy measurements.

Permeability is usually measured with multiple series of steady-state measurements at various pressure gradients. In this report, we describe a simple apparatus for an alternative approach to permeability measurement. This approach removes

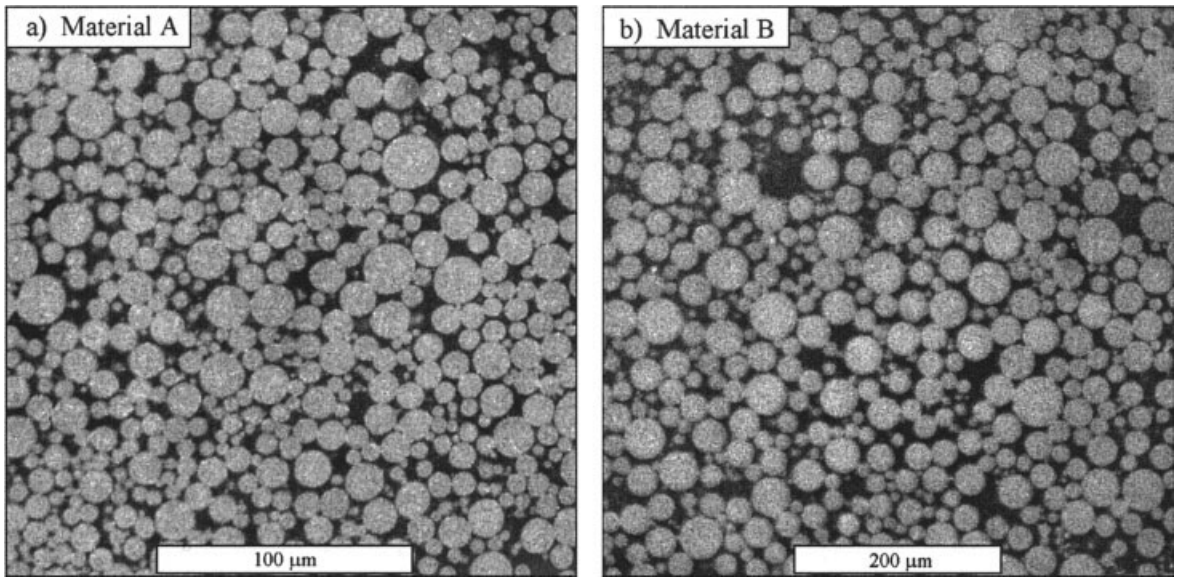

Figure 2. Fluorescence micrographs of 1-μm-thin sections of the materials shown in Figure 1 after flooding pores with Eosin stain and embedding in resin.

Note that resin-embedded pores are about 1.6 times as large as in aqueous media.

the need to adjust pressure settings between measurements, which can compromise the consistency of the sample fixture assembly. Our method requires only a single series of measurements for each sample, as measurements are recorded, whereas the two water levels of a water manometer equilibrate in response to an initial water head pressure differential.

Many researchers have sought ways to correlate pore size with permeability. Most of these efforts are based on capillaric models, where the porous medium is modeled by a series of channels or wormholes. Given that permeability has the dimension of length squared, it is generally presumed that the permeability must be proportional to the square of some characteristic length. This characteristic length, or "hydraulic radius," is presumed to be linked to the size of the capillaric channels to which the porous medium is assumed equivalent.

A widely accepted version of the hydraulic radius theory is known as the *Kozeny theory*. As Scheidegger (1974) details, the Kozeny theory involves simultaneously solving the Navier–Stokes equations for all capillaric channels passing through a cross-section normal to the flow in a porous medium. The resulting "Kozeny equation," given by the following equation,

$$k = \frac{cP^3}{S^2} \tag{2}$$

indicates that the permeability k is proportional to the cube of the porosity P and inversely proportional to the square of the specific surface S (the surface area per unit volume). The number c, called the "Kozeny constant," theoretically fluctuates very little and depends only on the cross-sectional shape of the capillary channels (such as $c = 0.50$ for a circle and 0.5619 for a square).

Many modifications to the Kozeny equation have been suggested. Most notably, it is clear that a factor to account for the degree of tortuosity of the flow path must be added. The result that the permeability is proportional to the square of a properly defined hydraulic radius has remained, but the form of the correct porosity factor is a source of much debate (Scheidegger, 1974).

Katz and Thompson (1986) used a semiempirical approach based on percolation theory and mercury intrusion porosimetry data to arrive at the following expression

$$k \approx \frac{l_c^2}{226F} \tag{3}$$

where l_c is the critical throat diameter obtained from the inflection point of a plot of percentage intrusion volume vs. pressure, and F is the formation factor, equal to the tortuosity divided by the porosity. The Katz–Thompson equation agrees extremely well with experimental data, and thus serves as a good starting point to relate permeability to pore size in a porous material. However, the materials studied in the historical development of hydraulic radius theory were usually composed of fused spheres or convex grains. Because the pore-structural geometry of sphere-templated porous materials—where porosity is high but pore throat size is relatively small—differs dramatically from that of previously studied materials, we expect that new modifications may be required to find a suitable correlation.

Experimental

Porous hydrogel fabrication

Crosslinked hydrogels were prepared by mixing 2-hydroxyethyl methacrylate (HEMA), ethylene glycol, water, tetraethylene glycol dimethacrylate, aqueous ammonium persulfate (40 g/100 mL), and aqueous sodium metabisulfite (15 g/100 mL) in a 10:3:2:0.46:1:1 ratio by volume. Poly(methyl methacrylate) (PMMA) microspheres (grade MB-8C or MB-20C;

Table 1. Embedding Procedure

Treatment	Time
70% ethanol with Eosin Y (1 g/L)	24 h
95% ethanol	15 min × 2
100% ethanol	30 min × 2
100% propylene oxide	15 min × 2
3:1 propylene oxide:polybed 812	3–4 h
2:1 propylene oxide:polybed 812	12–16 h
1:1 propylene oxide:polybed 812	12–16 h
100% polybed 812	8 h
Bake at 60°C	24 h

Sekisui Plastics, Tokyo, Japan) were stirred into the mixture at a concentration high enough to yield a slightly sticky dough (2.923 g/mL HEMA for MB-8C; 3.5 g/mL HEMA for MB-20C). The dough was pressed into 12-mL polypropylene test tubes, and air pockets between the dough and the tube wall were removed by puncturing the tube with a pin. Tubes were sealed and allowed to polymerize for 48 h. The gels were removed from the tubes by soaking in water. After ramping the soaking solution up to a 1:1 v/v acetone–water mixture (allowing at least 30 min per each 10% increment in composition for swelling to equilibrate), the gels were cut into slices of 1-mm thickness and punched into 9.5-mm disks. The soaking solution was then ramped at the same rate up to a 9:1 v/v acetone–water mixture. The PMMA template was removed with repeated extractions in 9:1 v/v acetone–water, with fresh solvent changes every 24 h. The removal of the PMMA from the gels was monitored by testing for turbidity after the addition of an equal volume of water to the replaced solvent.

Polymer embedding

Hydrated disks of porous poly–HEMA (~8 mm in diameter and 1 mm thick) were measured and subjected to the embedding schedule given in Table 1. After the embedding medium cured, the disk diameters were remeasured and the blocks were sectioned with a diamond-bladed microtome into 1-μm-thick sections.

Imaging equipment

Scanning electron micrographs were obtained using an FEI 2020 environmental SEM with an accelerating voltage of 15 kV and a chamber pressure of 0.67 kPa.

Fluorescence microscopy images were acquired on a Nikon Microphot–SA microscope with a plan apochromatic (Plan Apo) 20 × 0.75 NA objective and the 1.25 × magnification changer in place for the smaller pore material, and with a Plan Apo 10 × 0.45 NA objective for the larger pore material. Contrast was achieved with a cyan fluorescence filter set that allows excitation wavelengths of 430–450 nm and emission wavelengths of 460–480 nm. Image dimensions were calibrated with a stage micrometer.

Image processing

Processing steps on images of porous material cross sections were accomplished using Adobe Photoshop and the Image Processing Toolkit plug-in (Reindeer Graphics) with the following procedural sequence. For each material, a 1-megabyte, 8-bit fluorescence microscopy image of a cross section of the material displaying between 600 and 800 pore profiles was selected. Input brightness levels were expanded to the full range to enhance contrast, and noise was removed with a median rank filter of 1-pixel radius. Then a blurred background was created by applying a brightest neighbor filter of 45-pixel radius followed by a Gaussian blur filter of 45-pixel radius. After leveling the image by subtracting the blurred background and inverting, the leveled image was thresholded. The binary image was compared to a contrast-enhanced, leveled image (Figure 2), and the threshold level was adjusted until the feature dimensions were minimally affected by processing. A Euclidean distance map (where intensity is proportional to the distance from the phase boundary) and a corresponding ultimate point map (indicating maxima of the distance map) were created from the binary image, and the labels, positions, and intensity values for the ultimate points were exported to a Microsoft Excel spreadsheet.

Porosity

The porosity of the bulk material was determined by digitally measuring the area occupied by the void phase in the binary image of the plane section.

Pore size distribution

The ultimate point map (with feature identification numbers) was overlaid on the contrast-enhanced leveled image (Figure 2), and the locations of missing or extra points were noted where discrepancies were found, with careful attention to edges. This comparison also permitted the intensity values of the ultimate point map to be converted to actual pore profile diameters in microns. The ratio of the embedded sample disk diameter to the hydrated disk diameter was measured with calipers (and found to be 1.6), allowing the pore profile diameters to be scaled to aqueous media.

A pore profile size frequency histogram was constructed with 15 size categories, ranging from 0 to 15 μm for the smaller pore material (made with grade MB-8C porogens) and from 0 to 30 μm for the larger pore material (made with grade MB-20C porogens). The values of the histogram were normalized to a constant number of pixel increments per size category. The pore profile size frequency histogram was then multiplied by the 15 × 15 alpha matrix for sphere unfolding, shown in Table 2 (Cruz-Orive, 1976), to obtain the pore size frequency histogram.

Equation 4 defines the relationship between the measured circle size distribution and the spherical pore size distribution. Here, N_{Ai} is the number of circles per unit area in profile size class i, N_{Vj} is the relative number of spherical pores per unit volume in pore size class j, δ denotes the size category increment, and α_{ij} is the corresponding alpha matrix coefficient (Russ and DeHoff, 2000)

$$N_{Vj} = (1/\delta) \sum \alpha_{ij} N_{Ai} \tag{4}$$

Pore throat size distribution

A watershed filter was applied to the binary section image (creating boundaries between neighboring pore profiles), and this filtered image was subtracted from the unfiltered image. The resulting image contained only line segments, the lengths

Table 2. Size Distribution of Spherical Pores Is Calculated by Multiplying the Distribution of Circle Sizes in a Cross Section by this Alpha Matrix for Sphere Unfolding*

Circle Size Class	Sphere Size Class														
	1	2	3	4	5	6	7	8	9	10	11	12	13	14	15
1	2.00000	−0.68328	0.08217	−0.02799	−0.00048	−0.00298	−0.00126	−0.00094	−0.00062	−0.00045	−0.00034	−0.00026	−0.00020	−0.00016	−0.00013
2		0.89443	−0.47183	0.04087	−0.02528	−0.00393	−0.00427	−0.00234	−0.00167	−0.00117	−0.00087	−0.00066	−0.00051	−0.00040	−0.00033
3			0.66667	−0.39550	0.02903	−0.02416	−0.00516	−0.00488	−0.00288	−0.00208	−0.00150	−0.00011	−0.00087	−0.00069	−0.00055
4				0.55470	−0.34778	0.02308	−0.02293	−0.00565	−0.00512	−0.00315	−0.00230	−0.00169	−0.00129	−0.00101	−0.00080
5					0.48507	−0.31409	0.01947	−0.02176	−0.00582	−0.00518	−0.00327	−0.00242	−0.00180	−0.00139	−0.00109
6						0.43644	−0.28863	0.01704	−0.02071	−0.00584	−0.00516	−0.00332	−0.00248	−0.00186	−0.00145
7							0.40000	−0.26850	0.01527	−0.01977	−0.00579	−0.00509	−0.00332	−0.00250	−0.00189
8								0.37139	−0.25208	0.01393	−0.01893	−0.00571	−0.00501	−0.00330	−0.00250
9									0.34816	−0.23834	0.01287	−0.01818	−0.00560	−0.00491	−0.00327
10										0.32880	−0.22663	0.01200	−0.01751	−0.00549	−0.00481
11											0.31235	−0.21649	0.01128	−0.01691	−0.00538
12												0.29814	−0.20761	0.01067	−0.01636
13													0.28571	−0.19973	0.01015
14														0.27472	−0.19269
15															0.26491

*After Cruz-Orive (1976).

of which designate the widths of the necks wherever two circles (pore profiles) are joined. The identification numbers, positions, and lengths for these line segments were then exported to a Microsoft Excel spreadsheet. To account for any changes in neck size caused by applying the median rank filter, these sizes were calibrated against neck size measurements on the contrast-enhanced leveled image (Figure 2). The throat identification labels were then overlaid onto Figure 2 so that all extra pore throats could be identified and removed.

Because all of the pore throats are circular, the pore throats can be treated as oblate ellipsoids of revolution with eccentricity $e = 1.0$; that is, the pore throats are modeled as flat disks of zero thickness where the necks connecting the circles on the section image are chords through the disks. By modeling the pore throats in this way, the pore throat size distribution can be determined from the following equation, where N'_{Ai} is the relative number of necks per unit area in size class i, N'_{Vj} is the number of pore throats with diameter in size class j, and k_o is a correction factor that accounts for the eccentricity of the ellipsoids

$$N'_{Vj} = \left(\frac{1}{k_o \delta}\right) \sum \alpha_{ij} N'_{Ai} \tag{5}$$

For oblate ellipsoids, k_o is given by the following equation (Wicksell, 1926)

$$k_o = \frac{1}{2}\left(\sqrt{1 - e^2} + \frac{1}{e}\sin^{-1} e\right) \tag{6}$$

For eccentricity $e = 1.0$, evaluation of Eq. 6 gives $k_o \approx 0.7854$.

Pores per unit volume

The number of spherical pores per unit volume N_V is given by Eq. 7, where N_A is the number of circles (pore profiles) observed per unit area in the section, and r_o is the mean (number average) diameter of the spherical pores obtained from the pore size frequency histogram (Wicksell, 1925)

$$N_V = \frac{N_A}{r_o} \tag{7}$$

Pore throats per unit volume

The total number of pore throats per unit volume, N'_V, is given by Eq. 8, where N'_A is the number of necks per unit area in the section and r'_o is the mean (number average) pore throat diameter (obtained from the pore throat size frequency histogram)

$$N'_V = \frac{N'_A}{r'_0 k_o} \tag{8}$$

The average number of pore throats per pore n is then expressed as

$$n = \frac{2N'_V}{N_V} \tag{9}$$

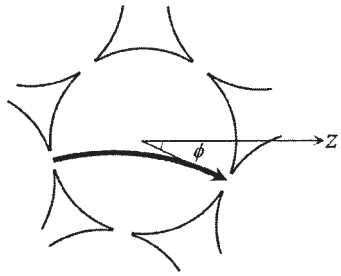

Figure 3. 2-D schematic of a spherical pore with pressure-driven flow in positive *z*-direction, showing average flow path and the angle ϕ between *z*-axis and center of pore throat with largest *z*-coordinate.

where the factor of 2 arises because each pore throat is shared by two adjoining pores.

Tortuosity: modeling the problem

The uniformity of pore shape in sphere-templated materials permits the tortuosity (as defined in Eq. 1) to be approximated when the average pore geometry is known. Because all pores are spherical in shape, we can find the effective transport path length L_e for a porous medium by determining the average relative path length of a fluid particle as it passes through a single pore.

We can model a spherical pore as a unit sphere centered at the origin, with the pressure-driven flow in the positive z-direction, as shown by the two-dimensional schematic in Figure 3. Because flow through porous media involves a small-length scale, the Reynolds number for most flow situations (such as during a permeability measurement) is small. At low Reynolds numbers, fluid flow is laminar along streamlines. As a fluid particle flows along the streamline of least resistance, it is most likely to enter a pore through the pore throat with the most negative z-coordinate, and most likely to exit the pore through the pore throat with the most positive z-coordinate. Such a flow path is illustrated in Figure 3. So we assume that the flow enters the pore through a primary entry pore throat and exits through a primary exit pore throat.

Nearly all other pore throats tend to be either oriented such that the flow is virtually parallel to the plane of the pore throat, or in a position nearly equivalent to that of the primary pore throat. In the first case, these pore throats contribute very little to the overall flow through the pore; in the latter case, the shape of the flow path will be similar to that of the primary flow path. Thus, it is reasonable to neglect the effects of "nonprimary" pore throats.

For low Reynolds numbers, the flow becomes fully developed almost immediately after entering the pore, so we can assume that the flow tends to pass through each pore throat in a direction normal to the circular throat. Furthermore, abrupt changes in curvature tend to be minimized in the streamlined flow. Based on these constraints, the average shape of the average flow path through a spherical pore can be closely approximated by an arc of constant curvature with ends normal to the inlet and exit pore throats. Figure 3 depicts a flow path with this shape.

Figure 3 also shows the angle ϕ_{max}, which represents the angle between positive z-axis and the line from the origin to the center of the pore throat with the most positive z-coordinate. The average value of ϕ_{max}, which we will denote as ϕ', is a function of n, the average number of pore throats per pore. If n is large, then ϕ' is close to zero, and the porous medium contains mostly straight transport pathways. Conversely, a small value of n corresponds to a large value for ϕ' and more tortuous transport pathways.

Tortuosity: determination of ϕ' by a Monte Carlo method

A Microsoft Excel macro was used to apply a Monte Carlo procedure to solve for ϕ' over the range of possible n values. For n number of pore throats per pore, the Monte Carlo program randomly selects n points on the surface of a unit sphere centered at the origin. Each point represents the center of a pore throat.

To select a random point on the surface of a sphere, the macro first chooses a random value of the azimuthal angle θ in spherical coordinates according to the following expression

$$\theta = 2\pi f \tag{10}$$

where f is the random number returned by the RAND( ) function such that $0 \leq f < 1$ and θ is in radians.

If the polar angle ϕ were also selected randomly, then the points near the poles would be overrepresented. To give each point on the surface of the sphere an equal probability of being selected, we must find a function to properly weight the selection of ϕ.

The fraction f of the surface of a sphere above a specified polar angle ϕ is given by

$$f = \frac{\int_0^{\phi} 2\pi R^2 \cdot \sin\phi \cdot d\phi}{4\pi R^2} = -\frac{1}{2}(\cos\phi - 1) \tag{11}$$

The weighting function for ϕ is found by inverting Eq. 11 to give

$$\phi = \cos^{-1}(1 - 2f) \tag{12}$$

To account for the average spatial effect of neighboring pores, whose spherical surfaces are assumed not to overlap, we must stipulate that the angle between the position vectors for each point must be at least $\pi/3$. This value for the "minimum spatially allowed angle" is based on the minimum for uniformly sized packed spheres (as illustrated in Figure 4). For each integer value of n, the macro repeatedly chooses points, rejecting those that do not meet the spatial constraint, until n points are selected; for two position vectors $\boldsymbol{a}$ and $\boldsymbol{b}$, the spatial constraint is given by

$$\frac{\boldsymbol{a} \cdot \boldsymbol{b}}{\cos|\boldsymbol{a}|\,|\boldsymbol{b}|} \geq \frac{\pi}{3} \tag{13}$$

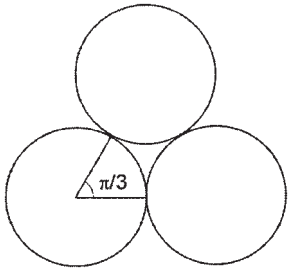

Figure 4. Minimum spatially allowed angle for uniformly sized packed spheres is $\pi/3$.

The maximum z-coordinate value ($\cos \phi_{max}$) is recorded, then the procedure is repeated for a large number of iterations to obtain an average value for $\cos \phi_{max}$, which we denote as $\cos \phi'$ in accordance with our earlier definition. The number of iterations depends on the level of accuracy required.

Tortuosity: calculation of α as a function of ϕ'

Once ϕ' is determined, we can calculate the average length of the chord C, which connects the inlet and exit points of the sphere. As shown in Figure 5, if the average inlet point A has Cartesian coordinates ($\sin \phi'$, 0, $\cos \phi'$), then the average position for the outlet point B lies on the circle in the plane $z = -\cos \phi'$.

The length of C is given by

$$C = \sqrt{C_x^2 + C_y^2 + C_z^2} = \sqrt{(\sin \phi' - \sin \phi' \cos \theta)^2 + (\sin \phi' \sin \theta)^2 + (2 \cos \phi')^2} \quad (14)$$

Equation 14 can be simplified to give

$$C = \sqrt{2 \cos^2 \phi' + 2 - 2 \sin^2 \phi' \cos \theta} \quad (15)$$

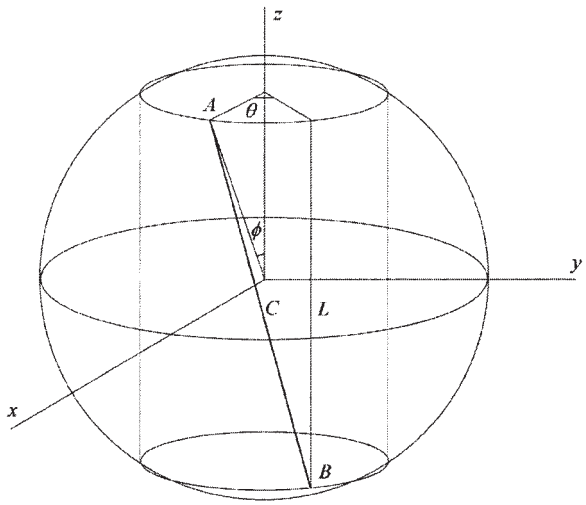

Figure 5. Unit sphere model of spherical pore, showing chord C connecting inlet and exit points for fluid particle.

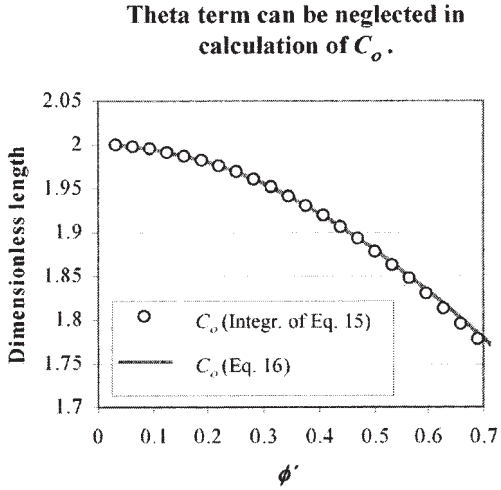

Figure 6. Comparison of Eqs. 15 and 16 for calculating C_o.

The mean value of C over the range $0 \leq \theta < 2\pi$ (which we will call C_o) can be calculated numerically. However, we expect that the term $2 \sin^2 \phi' \cos \theta$ is negligible because of the alternating sign of $\cos \theta$. Thus, Eq. 15 reduces to

$$C_o \approx \sqrt{2 \cos^2 \phi' + 2} \quad (16)$$

In Figure 6, Eq. 16 is plotted and compared to the C_o values obtained by numerical integration of Eq. 15. Figure 6 shows that, indeed, for ϕ' values $< \pi/4$, C_o can be approximated by Eq. 16 to within 0.5%.

Now the problem of calculating the effective relative path length L_e is reduced to two dimensions, as illustrated in Figure 7. As the figure shows, we can solve for L_e by introducing the two additional unknown dimensions β and r_2.

From the similar triangles in Figure 7, we write Eqs. 17, 18, and 19 to relate the three unknowns β, r_2, and L_e:

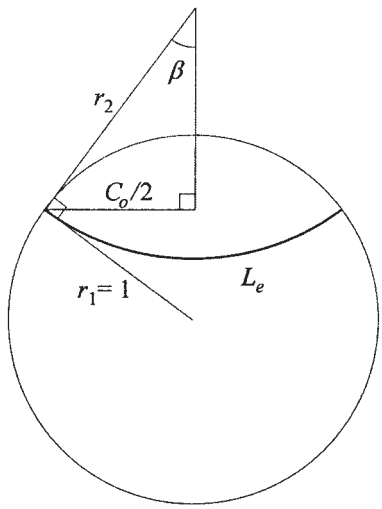

Figure 7. Geometric relationship between chord C_o and average relative path length L_e.

$$\cos\beta = \frac{C_o}{2} \tag{17}$$

$$\sin\beta = \frac{C_o}{2r_2} \tag{18}$$

$$L_e = 2r_2\beta \tag{19}$$

Solving for β, r_2, and L_e in terms of C_o gives

$$\beta = \cos^{-1}\frac{C_o}{2} \tag{20}$$

$$r_2 = \frac{C_o}{2\,\sin(\cos^{-1}C_o/2)} \tag{21}$$

$$L_e = \frac{C_o\cos^{-1}C_o/2}{\sin(\cos^{-1}C_o/2)} \tag{22}$$

Noting from Figure 5 that the straight-line path length L is equal to 2 cos ϕ' and combining Eqs. 1, 16, and 22 yields the tortuosity α as a function of ϕ':

$$\alpha = \left(\frac{\cos^2\phi' + 1}{2}\right)\left(\frac{\cos^{-1}\dfrac{\sqrt{2\cos^2\phi' + 2}}{2}}{\cos\phi'\sin\left(\cos^{-1}\dfrac{\sqrt{2\cos^2\phi' + 2}}{2}\right)}\right)^2 \tag{23}$$

Permeability measurements

For the flow of fluids in porous media, the hydraulic permeability k is defined by Darcy's law:

$$J_f = -\frac{k}{\eta}\nabla p \tag{24}$$

Here J_f denotes the fluid volume current density, η is the fluid viscosity, and p is the pressure field that drives the flow. The magnitude of J_f is called the Darcy velocity v_D (Wong, 1999).

The hydraulic permeability of each porous material was determined by plotting the Darcy velocity of water passing through the sample as a function of the pressure gradient. Figure 8 shows a schematic of the apparatus designed for these permeability measurements. To minimize evaporation, the top of each water column was covered except for a pinhole. A narrow 2-mL graduated pipet was used for the rising water column so that the flux could be measured accurately. A wider 10-mL graduated pipet was used for the falling water level column so that the water level would advance slowly for accurate water head measurements. The sample fixture was designed by modifying a tubing-connector assembly so that the sample disk could be supported at its perimeter and that the connector could be press-fitted, as shown in Figure 8, to eliminate leakage around the edge of the sample.

The two water levels were recorded at time intervals large enough to allow the water in the collecting column to advance approximately 1 cm. For each time interval, the average pressure gradient was plotted vs. the average Darcy velocity.

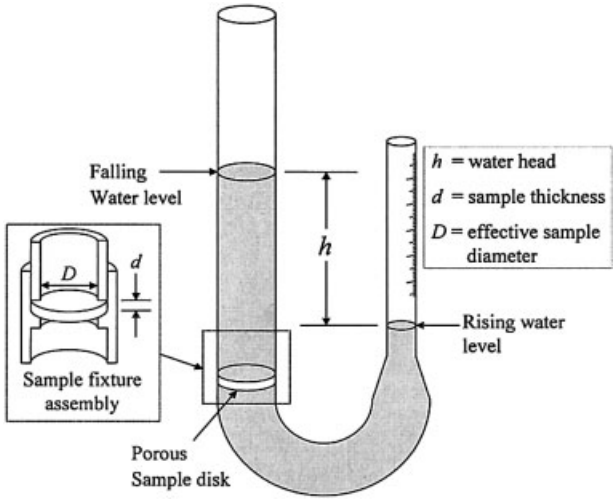

Figure 8. Apparatus for measurement of hydraulic permeability.

For each time step, the average Darcy velocity v_D (in μm/s) is given by

$$v_D = \frac{4(V_2 - V_1)}{\pi D^2(t_2 - t_1)} \times 10^4 \tag{25}$$

where $\Delta t = t_2 - t_1$ is the time step in seconds; V_1 and V_2 are the respective volumes in milliliters, read off the graduated collecting column at times t_1 and t_2; and D is the effective sample diameter in centimeters (that is, the diameter of the cross-sectional sample area available for transport).

The average pressure gradient in kPa/cm, ∇p, is given for each time step by

$$\nabla p = \frac{\rho g\bar{h}}{d} \times 10^{-4} \tag{26}$$

where ρ is the mass density of water at room temperature in g/cm^3 (0.998), g is the acceleration of gravity in cm/s^2 (981), d is the sample thickness in cm, and $\bar{h}$ is the average water head (in cm) for the time step $\Delta t = t_2 - t_1$, given by

$$\bar{h} = \frac{h_1 - h_2}{\ln(h_1/h_2)} \tag{27}$$

where h_1 and h_2 are the water heads at times t_1 and t_2 (in cm), respectively. The log mean water head is used because the water head decays monoexponentially when Darcy's law is obeyed.

The hydraulic permeability k in cm^2 was then calculated from

$$k = \frac{\eta}{m} \times 10^{-10} \tag{28}$$

where η is the viscosity of water at room temperature in mPa·s (0.96) and m is the slope of the ∇p vs. v_D plot at the limit of $\nabla p \rightarrow 0$, with ∇p in kPa/cm and v_D in μm/s. Measuring the slope at the limit of zero stress eliminates the need to account for mechanical distortion of the porous sample.

Specific surface area

Equation 29 was used to calculate the specific surface area S

$$S \approx \pi r_o^2 N_V - \frac{\pi}{2} r_o'^2 N_V' \tag{29}$$

The subtracted term in Eq. 29, equal to twice the cross-sectional area of the pore throats, is a good approximation for the reduction in pore surface area attributed to the presence of the pore throats.

Effective transport porosity

We can define an effective transport porosity P' as the average fraction of a spherical pore's surface area that is occupied by pore throats. The value of P' can be calculated from parameters we have already determined stereologically. Accordingly, the effective transport porosity P' was calculated from

$$P' \approx \frac{\frac{\pi}{2} r_o'^2 N_V'}{\pi r_o^2 N_V} = \frac{n r_o'^2}{4 r_o^2} \tag{30}$$

Results and Discussion

Figure 1 shows SEM images of cross sections of the two sphere-templated porous poly–HEMA hydrogel materials analyzed in this report. Hereafter, we will refer to the smaller pore material as Material A and the larger pore material as Material B. The spherical pore shape is less obvious in Figure 1a because the material cross section was cut before the porogens were removed, yielding a more irregular surface. In both images, the dark circular pore throats that connect neighboring pores are visible.

Figure 2 shows fluorescence micrographs of 1-μm-thick plane sections of Materials A and B. The two phases are clearly distinguishable. The presence of solely circular pore profiles in the image is consistent with the expectation of spherical pore geometry. As expected from knowledge of the material fabrication method, none of the circles overlaps. Nearly all of the circles connect to one or more neighboring circles. Each of these necks represents the profile of a pore throat.

Quantitative results summary

The quantitative results for Materials A and B are summarized in Table 3.

Table 3. Quantitative Results Summary

Property	Material A	Material B
P	0.64	0.67
N_A (μm^{-2})	0.0312	0.00525
N_V (μm^{-3})	0.00798	0.000521
r_o (μm)	3.90	10.1
N_A' (μm^{-2})	0.0300	0.00438
N_V' (μm^{-3})	0.0277	0.00147
r_o' (μm)	1.38	3.79
n	6.94	5.64
α	1.34	1.46
S (cm^{-1})	1.20×10^4	5.30×10^3
P'	0.217	0.201
k (cm^2) measured by perfusion	1.2×10^{-11}	8.3×10^{-11}
k (cm^2) predicted by Eq. 31 (modified Katz–Thompson eq.)	1.3×10^{-11}	8.7×10^{-11}
k (cm^2) predicted by Kozeny eq.	1200×10^{-11}	7000×10^{-11}
k (cm^2) predicted by modified Kozeny eq. with P'	48×10^{-11}	190×10^{-11}

Porosity

The accuracy of the porosity measurements was limited by the difficulty in determining the exact boundary between the two phases. The slight blurring of the phase boundary is attributed not to the resolution limit, but rather to the fact that the examined section was not ideally thin. This is suggested by the observation that the edges of smaller circles are generally much blurrier than those of larger ones. When the section cuts through a spherical pore near its equator, as is the case with the largest circles, the boundary of the circle appears sharp because the phase boundary is nearly perpendicular to the plane of the section. Because of the spherical pore geometry, the boundary position difference between the top and bottom of the section can be up to several microns when the section cuts through the edge of a large pore.

Pore size distribution

Figure 9 shows the pore size frequency histograms for Materials A and B. The size distribution of pore profiles in a random section does not directly correspond with the size distribution of the spherical pores for two reasons. For one, the circle created by a random cut through a sphere will always have a smaller diameter than the sphere it represents unless it perfectly bisects the sphere. Second, larger spheres have a greater probability than smaller spheres of being cut by a random section.

Pore throat size distribution

Figure 9 also shows the pore throat size frequency histograms for Materials A and B. To our knowledge, this is the first time that pore throat size distributions have been determined stereologically from quantitative microscopy measurements. Because a median rank filter was required for adequate thresholding, the throat profile sizes needed to be carefully calibrated against measurements on the original image, and inspection of the computer-aided feature count showed that a significant number of excess throats needed to be deleted. This difficulty can be minimized with a higher-resolution image, so that noise reduction can be accomplished with minimal effect on throat profile dimensions.

Permeability measurements

Figure 10 shows permeability data for Materials A and B. The permeability k is given by the slope at the limit of $\nabla p \rightarrow 0$.

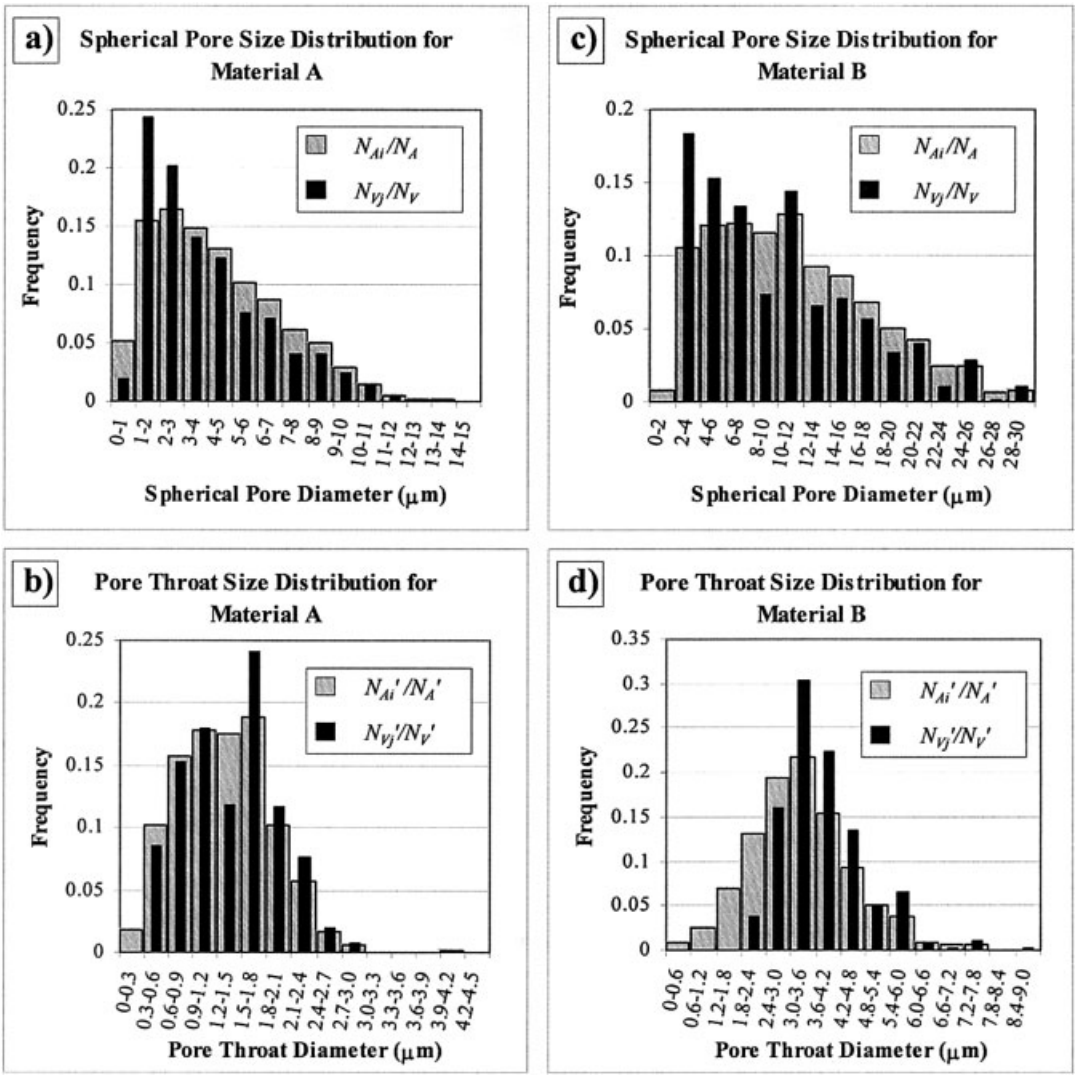

Figure 9. Pore size distributions.

Tortuosity results

Equation 23 is significant because we now have an explicit expression for the tortuosity α in terms of a single variable, ϕ'. Because ϕ' is presumed to be a function of only n, we can now determine the tortuosity of a porous medium with spherical pores, starting from only parameters measured easily by quantitative microscopy techniques.

Although it is theoretically possible to fabricate a sphere-templated material with n approaching 12 if the material is made with highly monodispersed spheres arranged with perfect close-packed crystal-like order, values of $n > 10$ do not occur in randomly oriented pore structures because of the spatial constraint, and the Monte Carlo algorithm is limited to $n \leq 10$ for the same reason (computer processing time approaches infinity for $n > 10$).

The Monte Carlo procedure was applied for n values 2 through 10. In each case, 100,000 iterations were sufficient to yield a 95% confidence interval for cos ϕ' of $<0.2\%$. In Figure 11, cos ϕ' and α, as determined by the methods presented herein, are plotted as functions of n.

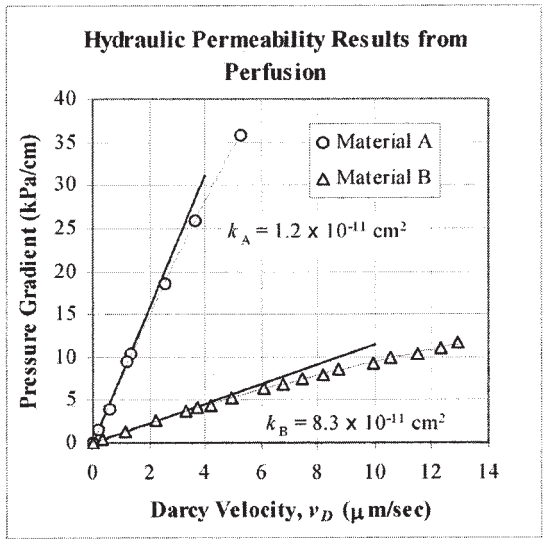

Figure 10. Darcy velocity is plotted vs. the pressure gradient to obtain the permeability.

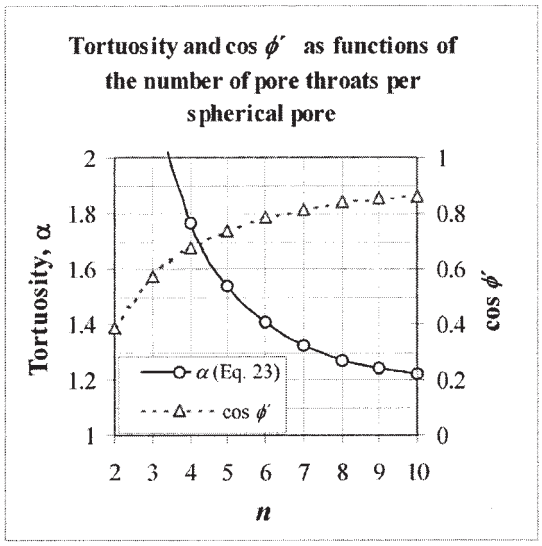

Figure 11. Tortuosity α is plotted as a function of number of pore throats per spherical pore (from Eq. 23).

Results of the Monte Carlo method for determining cos ϕ' are also shown.

Relating pore size to permeability

In relating the pore size of a porous material to its permeability, we can choose any of a number of relationships available in the literature. We choose to use Eq. 3 because it has been shown to agree well with experimental data. However, we must consider an important difference between the spherically pored materials analyzed herein and the fused bead materials on which the correlation of Eq. 3 was tested. For spherically pored materials, we must account for the fact that the size of the pore throats is much smaller than that of the pores. Thus it is appropriate to make an adjustment to the porosity. With the effective transport porosity P' (as we defined earlier in the experimental section) replacing the absolute porosity P, and the mean pore throat diameter r'_o replacing the critical throat diameter l_c, the correlation in Eq. 3 now becomes

$$k \approx \frac{r'^2_o P'}{226\alpha} \tag{31}$$

In Table 3, it is evident that the permeability predicted by Eq. 31 gives excellent agreement with our perfusion data for both materials analyzed.

The close agreement of stereologically determined permeability predictions with perfusion data, coupled with the highly symmetrical shape of the pore throat size distributions, suggests that r'_o is a good approximation for the most-probable throat diameter, a good indicator of network conductance (Wong, 1999). The result also provides supporting evidence that our tortuosity and effective transport porosity estimates are reasonably accurate. The results for tortuosities obtained with the methods presented herein have yet to be compared to results obtained by experimental resistivity measurements. Such a comparison would undoubtedly be useful in examining the accuracy of the method.

For porous materials composed of fused beads or packed beds, the constrictions in the transport pathways are almost as large as the pores. So for these materials, the absolute porosity P is nearly equivalent to our newly defined effective transport porosity P'; and as we have discussed, relationships between P and permeability have already been established. Therefore, the use of an effective transport porosity as we have defined it in this report would seem to be applicable to most classes of porous media, and not only to sphere-templated porous materials.

We can also compare our results with an appropriate form of the Kozeny equation. We see in Table 3 that the permeability predicted by the Kozeny equation (that is, Eq. 2 divided by a tortuosity factor L_e/L) diverges from the measured permeability by three orders of magnitude when the absolute porosity P is used. However, substituting the effective transport porosity P' into the same tortuosity-adjusted Kozeny equation gives permeability values that agree much better with the measured values. Because the result given by this modified Kozeny equation depends on the cube of P', the result is sensitive to small errors in pore throat size measurement. Moreover, $1/S$ is not a reasonable choice for the hydraulic radius when the constrictions in the transport pathways are much smaller than the pore spaces. Accordingly, the Kozeny equation appears less suitable than Eq. 31 for predicting permeability.

Conclusions

We have developed a useful approach for the quantitative characterization of the pore structure of sphere-templated porous media. The approach can be applied to other porous materials with similar pore structures consisting of interconnected spherical voids.

Notably, we have expanded on a previously known sphere unfolding technique; we have shown that the technique can be successfully extended to yield pore throat size distributions. This approach can eliminate the need for expensive pore-probing instrumentation.

For the transport properties of a porous material to be quantitatively related to its pore structure and pore size distribution, a quantitative determination of the tortuosity is essential. We have developed an innovative method that permits the estimation of the tortuosity for spherically pored materials from stereological interpretation of quantitative microscopy measurements. Because of the relative difficulty and unreliability associated with determining tortuosity by resistivity measurements or other means, the method presented in this report should be considered a valuable alternative.

We have also introduced a new and simple apparatus for measuring the hydraulic permeability. Our novel approach requires no special or expensive equipment and can greatly simplify the acquisition of perfusion data.

Finally, we have demonstrated that quantitative microscopy coupled with stereological interpretation can be used to predict the permeability of these porous materials. Furthermore, our modification to existing hydraulic radius theory helps to generalize existing pore size–permeability correlations so that they are appropriate for sphere-templated porous structures.

Acknowledgments

This research was supported by Bioengineered Materials ERC at the University of Washington (UWEB), National Science Foundation Grant EEC-9529161, and National Institutes of Health Grant R24HL-64387. Microspheres were generously donated by Sekisui Plastics. The assistance of L. Martinson, L. Muffley, R. Underwood, F. Marshall, and K. Hauch is gratefully acknowledged.

Literature Cited

Bear, J., "Hydrodynamic Dispersion," *Flow Through Porous Media*, R. J. M. De Wiest, ed., pp. 109–196, Academic Press, New York (1969).

Collins, R. E., "Statics of Fluids in Porous Media," *Flow of Fluids through Porous Materials*, R. E. Collins, ed., pp. 22–46, Van Nostrand Reinhold, New York (1961).

Cruz-Orive, L.-M., "Particle Size-Shape Distributions: The General Spheroid Problem," *J. Microsc.*, **107**, 235 and **112**, 253 (1976).

Harris, L. D., B. S. Kim, and D. J. Mooney, "Open Pore Biodegradable Matrices Formed with Gas Foaming," *J. Biomed. Mater. Res.*, **42**, 396 (1998).

Hua, F. J., G. E. Kim, J. D. Lee, Y. K. Son, and D. S. Lee, "Macroporous Poly(L-lactide) Scaffold. 1. Preparation of a Macroporous Scaffold by Liquid–Liquid Phase Separation of a PLLA–Doxane–Water System," *J. Biomed. Mater. Res.*, **63**, 161 (2002).

Katz, A. J., and A. H. Thompson, "Quantitative Prediction of Permeability in Porous Rock," *Phys. Rev. B*, **34**, 8179 (1986).

Ma, P. X., and J. W. Choi, "Biodegradable Polymer Scaffolds with Well-Defined Interconnected Spherical Pore Network," *Tissue Eng.*, **7**, 23 (2001).

Marshall, A. J., and B. D. Ratner, "Quantitative Microscopy for Analysis of Hydrogel Pore Structure," *Proc. Microsc. Microanal.*, Vol. 7, Supplement 2, 834 (2001).

Russ, J. C., and R. T. DeHoff, eds. *Practical Stereology*, pp. 250–255, Plenum Press, New York (2000).

Scheidegger, A. E., "Physical Aspects of Permeability," *The Physics of Flow through Porous Media*, A. E. Scheidegger, ed., pp. 124–151, University of Toronto Press, Toronto, Canada (1974).

Wicksell, S. D., "The Corpuscle Problem: A Mathematical Study of a Biometric Problem," *Biometrika*, **17**, 84 (1925).

Wicksell, S. D., "The Corpuscle Problem: Second Memoir: Case of Elliptical Corpuscles," *Biometrika*, **18**, 151 (1926).

Wong, P.-Z., "Conductivity, Permeability, and Electrokinetics," *Methods in the Physics of Porous Media*, P.-Z. Wong, ed., pp. 119–160, Academic Press, San Diego, CA (1999).

Yang, S. F., K. F. Leong, Z. Du, and C. K. Chua, "The Design of Scaffolds for Use in Tissue Engineering. Part 1. Traditional Factors," *Tissue Eng.*, **7**, 679 (2001).

Yortsos, Y. C., "Probing Pore Structures by Sorption Isotherms and Mercury Porosimetry," *Methods in the Physics of Porous Media*, P.-Z. Wong, ed., pp. 69–118, Academic Press, San Diego, CA (1999).

Manuscript received Dec. 17, 2003, and revision received Aug. 5, 2004.